International Journal of Infrared and Millimeter Waves
https://doi.org/10.1007/s10762-019-00636-7

Terahertz Spectroscopy and Density Functional Theory Investigation of the Dipeptide L-Carnosine

Jens Neu[1] · **Charles A. Schmuttenmaer**[2]

Received: 28 June 2019 / Accepted: 17 October 2019 / Published online: 27 February 2020

Abstract

Terahertz spectroscopy and density functional theory (DFT) calculations have been used to study the dipeptide L-carnosine. In this paper, we expand the range of materials described with THz measurements and DFT calculations from amino acids to dipeptides. Three clear resonances were detected in the experimental spectrum at 1.5 THz, 1.9 THz, and 2.3 THz. Additionally, we performed periodic boundary condition DFT calculations. The computational spectrum accurately reproduces the experimental one.

Keywords Terahertz spectroscopy · Density functional theory · Peptides · Carnosine

1 Introduction

In this paper, we present THz spectra of L-carnosine, a dipeptide. This dipeptide is naturally occurring in muscles where it acts as a pH buffer [1, 2]. Furthermore, L-carnosine is explored for its potential in therapeutics, targeting age-related illnesses [3, 4]. As a dipeptide, it is an excellent model system to validate that DFT calculations which were previously used to describe amino acids are valid for larger systems.

The range of materials that can be identified using THz spectroscopy is constantly expending: covering artificial metamaterials [5–10, 10, 11], illegal drugs [12–14],

Electronic supplementary material The online version of this article (https://doi.org/10.1007/s10762-019-00636-7) contains supplementary material, which is available to authorized users.

✉ Jens Neu
jens.neu@yale.edu

Charles A. Schmuttenmaer
Charles.Schmuttenmaer@yale.edu

[1] Department of Molecular Biophysics and Biochemistry, and Molecular Science Institute, Yale University, West Haven, CT, 06516, USA

[2] Department of Chemistry, and Energy Science Institute, Yale University, New Haven, CT, 06520-8107, USA

explosives [13, 15], and organic molecular crystals [16–21]. Molecular crystals are of crucial importance in pharmaceutical products as the crystallinity can have an influence on the biochemical activity of these materials [22].

The measured spectral features can be used to identify the materials. However, in contrast to IR spectroscopy in which a spectral feature can easily be assigned a particular stretch or bend mode, THz resonances are delocalized over a large number of atoms within the unit cell. This delocalization makes it impossible to simply assign a resonance at a certain THz frequency to a particular movement. While this seems to be a disadvantage, it is actually one of the strengths of THz spectroscopy. A delocalized mode is intrinsically sensitive to small and minor changes in the material. For example, THz spectroscopy can be used to distinguish different polymorphs [18, 23], or single atom replacements which are hard to detect with crystallographic techniques [24].

Density functional theory (DFT) calculations are needed to understand these delocalized modes. These calculations have been performed for a large range of materials [18, 23, 25–30]. The simplest systems studied are amino acid crystals made up of a single amino acid unit [19, 23, 24, 31, 32]. Amino acids are an excellent model system to explore the accuracy of THz–DFT calculations, and the insight gained from them has significantly improved the accuracy of DFT spectra.

In recent years, more complex materials systems have been explored using a combination of DFT and THz spectroscopy [17, 25, 27, 33]. Peptides are biopolymers composed of two or more amino acids which form a chain. Naturally, their structure and dynamics are more complicated than single amino acids, but it is now possible to probe them experimentally and computationally.

This paper first describes sample preparation and THz spectrometer. Then, the experimental spectra are presented. The next two sections describe the DFT methods and results. The final section is the conclusion.

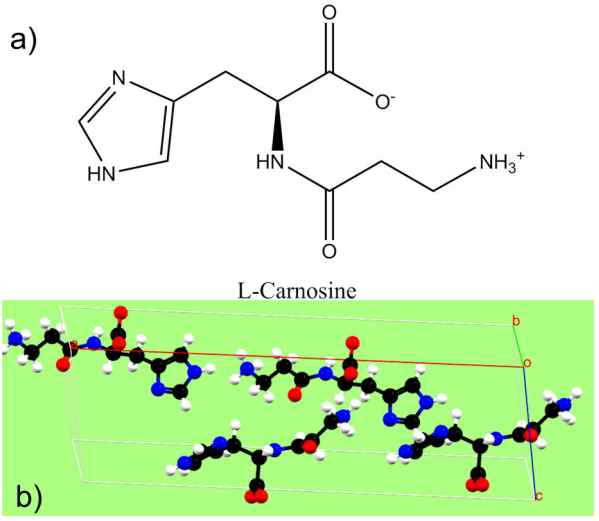

Fig. 1 **a** Molecular structure of L-carnosine. **b** Packing of the dipeptide in the unit cell. The unit cell is visualized using Mercury, and the corresponding CCSD entry is BALHIS01[37]

2 Sample Preparation and THz Spectrometer

β-Alanyl-L-histidine, common name L-carnosine, was purchased from Sigma–Aldrich (purity 99%). The structure and unit cell of this dipeptide are shown in Fig. 1. The material was ball-milled for 3 min to ensure a micro-granular sample material. The resulting powder was characterized using powder X-ray diffraction (PXRD) (see Fig. 3) to confirm that the material is in fact crystalline and not amorphous. The powder was then mixed with Teflon powder, purchased from Santa Cruz Biotechnology. This powder was stored under dry air to minimize water content in the pellets. The four pellets that were studied contained 31 ± 5 mg, 52 ± 5 mg, 85 ± 5 mg and 101 ± 5 mg respectively of L-carnosine in approximately 1000 mg Teflon. After mixing, the material was compressed at a pressure of 11 kbar for 2 s. The resulting pellets had a thickness of 3.7 mm and a diameter of 13 mm.

The mixed pellet is mounted in a nitrogen sample-in-vapor cryostat with a temperature control unit. The sample temperature is measured with one sensor below the sample and one above. When both temperature sensors have reached the same value, the measurement commences. The temperature range of the cryostat is 300 K to 65 K, with an accuracy better than 5 K.

The cryostat is placed in a THz–time domain spectrometer (TDS)[34], and the sample is placed at the focal point of the off-axis paraboloidal mirrors. The spectrometer is based on a KM Labs Griffin oscillator emitting laser pulses centered around 810 nm, with a repetition rate of 90 MHz, an average power of 250 mW, and a pulse length of sub 30 fs. This beam is split into THz generation and detection beams. The generation beam is focused onto an interdigitated antenna (Batop GmbH), which is biased with +/- 10 V square function with a modulation frequency of 4.2 kHz [8]. This frequency is used as the reference frequency for a lock-in amplifier (SRS-830). The detection beam gates a dipole antenna with a 5-μm gap. The resulting bandwidth covers the range of 0.2 to 3.5 THz. However, the cryostat uses Teflon outer windows and quartz inner windows, which limits the high-frequency transmission and truncates the useable spectral range to approximately 2.5 THz.

3 Experimental Results

For each measurement, the THz transmission without pellet and with pellet is measured. From these measurements, the complex-valued transmittance of the pellet is determined. The transmission is then used to calculate the complex refractive index n_{pellet} as described in detail in previous publications [23, 34]. This value, however, is a property of the pellet and not the dipeptide itself.

The dipeptide properties are extracted from those of the pellet using effective medium theory (EMT). In this case, Maxwell–Garnett EMT is used as follows [35]:

$$\frac{\epsilon_{\text{pellet}} - \epsilon_{\text{T}}}{\epsilon_{\text{pellet}} + 2\epsilon_{\text{T}}} = f\frac{\epsilon_{\text{pep}} - \epsilon_{\text{T}}}{\epsilon_{\text{pep}} + 2\epsilon_{\text{T}}} \tag{1}$$

with pep denoting peptide properties and T the properties of the Teflon host material. f is the volume filling factor and we used $n^2 = \epsilon$ for nonmagnetic material. In

addition, we also applied the Bruggeman EMT theory [36] which yielded identical results within the measurement uncertainty.

The absorption coefficient of L-carnosine is plotted in Fig. 2, for room temperature (red line), at 100 K (purple line) and for 65 K (blue line). The shading around the lines illustrates the standard deviation. The standard deviation is calculated based on four different pellets, with different mixing ratios as listed in the Supplementary Information. These samples were each measured at three different positions to verify the homogeneity of the pellet.

The room temperature measurement shows three broad absorption features located slightly above 1.5 THz, at 1.8 THz, and around 2.5 THz. The width of these features makes a clear identification challenging. The width of these resonances is caused primarily by thermal broadening. Room temperature (300 K) corresponds to thermal photons of 26 meV≈6.3 THz. Therefore, the spectral features are not describing transitions solely from the ground state of the resonant mode, but from thermally occupied modes as well. As most potentials exhibit anharmonicity, the excitation from the ground state ($\nu = 0$) to the first excited state ($\nu = 1$) has a slightly different energy than an excitation from the first ($\nu = 1$) to the second ($\nu = 2$) excited state, and so on. The measured absorption is an average over all transitions from occupied states which causes the observed broadening.

The samples were then cooled down to 100 K, which reduces the thermal occupation of excited modes. This freezing out of phonons results in a sharpening of the resonant absorption profile (purple line). The spectrum at reduced temperatures shows three clear resonances: One close to 1.5 THz, one slightly below 2 THz, and one at 2.4 THz. To confirm the validity of these resonances, the sample temperature was decreased again.

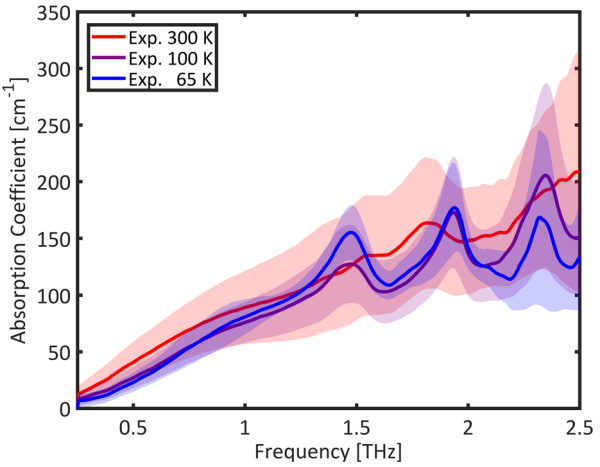

Fig. 2 Absorption coefficient of L-carnosine, determined from the transmission measurements using EMT. The spectrum was collected at room temperature (300 K, red line) and at cryogenic temperatures (100 K purple and 65 K blue). The absorption features are more pronounced at lower temperature as the thermal occupation of the modes is decreased. The shading visualizes the standard deviation between four samples and three positions on each of the samples

The sample was cooled to 65 K using evaporative cooling, a technique in which liquid nitrogen is sprayed into an evacuated chamber. The low pressure reduces the liquid gas transition temperature and allows to reach temperatures below the boiling point of nitrogen of 77 K. The low temperature spectrum clearly shows the same resonances as in the one at 100 K. The peak positions of this measurement are summarized in Table 2, which also presents the results of the DFT calculations.

4 Density Functional Theory Calculation Methods

Experimental THz spectroscopy is an excellent technique to probe low-frequency modes of many different materials, including energetic materials in a non-contact and safe manner [38], pharmaceuticals, and organic compounds [39, 40]. However, detecting resonant excitations is only the first part of the story. The second part is to understand the underlying atomic motions contributing to a particular mode. This is challenging in the THz spectral range because a clear assignment is not possible as is the case with IR spectroscopy. Ultimately, the experimentally observed absorptions are best modeled with periodic boundary DFT calculations.

DFT spectral calculations begin with the atomic coordinates within the unit cell. The crystal structure was previously reported (CCSD BALHIS01 [37]), and we confirmed the accuracy of this structure using powder X-ray diffraction (PXRD) (see Fig. 3).

The structural parameters are imported into Siesta-4.0-530. Siesta (Spanish Initiative for Electronic Simulations with Thousands of Atoms) [41] is a free software package providing an easy access to the field of computational chemistry with a minimal financial burden. The software supports the optimization and energy minimization of solid-state materials utilizing periodic boundary conditions, as well as providing the spectra of these materials.

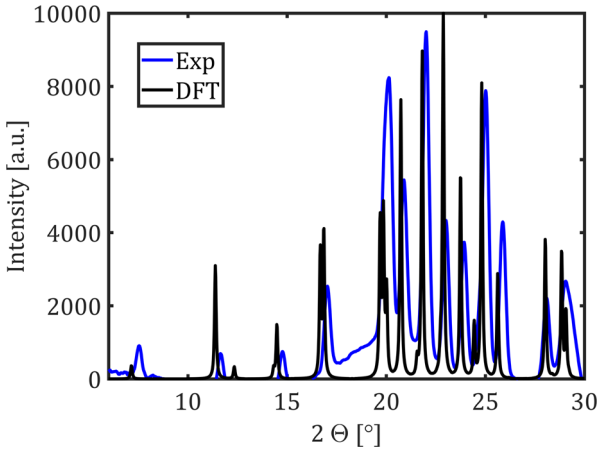

Fig. 3 PXRD spectrum of ball-milled L-carnosine (blue line) compared to that calculated from the structure determined after DFT optimization

The THz calculations utilized vdW-DF-cx functionals [42], based on generalized gradient approximation (GGA) level exchange–correlation functionals. These functionals account for van der Waals (vdW) forces, which are extraordinarily important for low-energy excitations, such as THz modes. The vdW forces are implemented using the Lundqvist–Langreth nonlocal density–density interaction framework [43]. The system furthermore uses a triple zeta, doubly polarized (TZDP) basis set. (The input files as well as the used pseudopotential are found in the Supplementary Information of this manuscript). It is important to stress that functionals should always be tested intensively with well-studied materials, before applying them to novel materials [19, 23, 24, 44]. These tests should involve deuteration, and will also provide a reasonable range for the scaling factors.

The first step of the calculation is to relax the geometrical parameters. The unit cell parameters as well as the coordinates of the individual atoms are optimized to minimize the energy and the remaining stress in the system [19, 31]. By definition, this type of calculation is at a temperature of 0 K. Thus, all phonons in the system are in the ground state; hence, it cannot reproduce the broadening observed in the experimental spectra as a funtion of increasing temperature. The optimized structure was within 1.6 % of the input geometry (see Table 1 for tabulated values). The second step after optimizing the structure is to verify that the calculated geometry is in agreement with the experimental one by comparing their PXRD spectra. These are plotted in Fig. 3 where the blue line is for the experimental spectrum and the black line is for the calculated spectrum. All features are reproduced, and other than a systematic error due to sample position and/or thickness, there is excellent agreement with the experimental data. The PXRD measurements verify that the material has crystallized in the same polymorph as BALHIS01.

After the accuracy of the unit cell calculation has been verified, the THz spectrum is calculated. This is done by first displacing each atom individually and calculating the resulting force matrix, as well as the polarization matrix. The force matrix reveals the mechanical resonances of the system. In addition to the calculated resonance frequency, we calculate the IR intensity of the mode. This is achieved using the Berry phase approach to calculate the macroscopic polarization [45]. Using the calculated polarization, the Born effective charge tensor of each atom is calculated [46]. This

Table 1 Unit cell geometry of the original CCSD cell, and the DFT optimized cell

	Balhis01	DFT	Difference (%)
a (Å)	24.7	25.1	1.6
b (Å)	5.43	5.38	− 0.9
c (Å)	7.99	7.88	− 1.4
α (°)	90	90	0
β (°)	100.12	100.23	0.1
γ (°)	90	89.99	− 0.01
V (Å^3)	1056	1047	0.9

tensor describes the dipole transitions upon photoexcitation and provides the THz intensity of each mode [23, 45].

The structural optimization of L-carnosine took 3,840 CPU hours. The THz spectra calculation, including the single atom displacement took 21,000 CPU hours in total. Both calculations were performed on the Yale HPC cluster utilizing 20 GB memory.

5 Density Functional Theory Calculation Results

The resonance frequency depends on the basis set and pseudopotentials chosen, and DFT calculations often overestimate the resonance frequency [23–25, 39, 47]. It is quite common to scale the frequencies by factors ranging from 0.9 to 1.05 [39, 47]. Therefore, to achieve a more accurate description of the experimental results, the calculated frequencies were scaled by 0.9.

DFT calculations do not provide the width of the resonances. In general, this width will depend on thermal broadening but also on crystal impurities and lattice defects. Hence, it would be possible to choose an individual resonance width for each absorption feature. However, we present the results using the same fixed width of 0.25 THz for each resonance to minimize assumptions and fit parameters. The experimental spectrum measured at 65 K is plotted in blue along with the calculated one (black) in Fig. 4.

We note an excellent agreement in the spectral range above 1 THz and up to the noise floor of the spectrometer (2.5 THz). The three experimental peaks at 1.48 ± 0.02 THz, 1.93 ± 0.04 THz, and 2.27 ± 0.11 THz are reproduced in the DFT calculations at 1.45 THz, 2.00 THz, and 2.42 THz, summarized in Table 2.

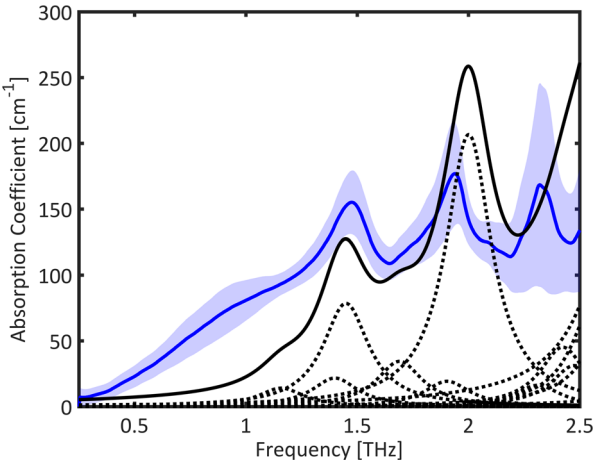

Fig. 4 Absorption coefficient of L-carnosine measured at 65 K (blue) compared to the results of the DFT calculation (black). The calculated absorption frequency is scaled by a factor of 0.9, and the resonances are convoluted with a Lorentzian function with a width of 0.25 THz. The dashed lines show the absorption of individual DFT resonances

Table 2 Comparison between experimental resonances and calculated resonance frequency

Experimental results	DFT	DFT inensity (cm^{-1})
	1.40 THz	35
1.48 ± 0.02 THz	1.45 THz	128
	1.9 THz	32
1.94 ± 0.02 THz	2.00 THz	336
	2.3 THz	26
2.38 ± 0.05 THz	2.4 THz	73
	2.48 THz	51
	2.57 THz	129
2.61 ± 0.08 THz	2.7 THz	187
	2.8 THz	883

The calculation also shows a very strong feature near 2.5 THz. This is caused by the superposition of multiple modes at similar frequencies. In general, it is challenging to accurately reproduce broadening and resonance strength of all modes simultaneously. Some modes are more sensitive to lattice defects and will broaden more strongly than other ones. As no crystal is perfect, this will shift the relative strength or width of modes compared to each other. This results in an overall overestimation of the high-frequency resonances, while the lower frequency ones are captured accurately.

In addition to the three major resonances, there are many weaker resonances in the simulation results which contribute to the broadening of the spectrum and shoulders on some peaks.

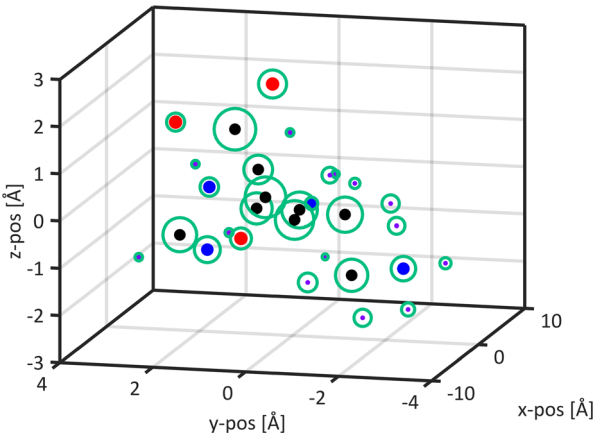

Fig. 5 Illustration of the atom displacements evaluated at the 2 THz mode. This mode displaces essentially all atoms within the molecule and unit cell, which is common for low frequency modes. For clarity, the absolute value of the displacement vector is used, as represented by a sphere, and scaled up by a factor of 500

As stated above, it is not possible to describe low-frequency THz modes as a rock or bend or stretch, etc., as is done with IR modes. They all involve most or all of the atoms in the unit cell. There are a number of ways to interpret and compare these modes, however [19, 24, 31].

One is to plot the atomic displacements at a particular resonance frequency, as done in Fig. 5. Many authors display these displacements with arrows, highlighting the directionality of the movement, but these can be difficult to interpret at times since arrows pointing in three dimensions are being plotted in a two dimensional figure. However, for many analyses, the direction is less important than the magnitude of displacement which is a measure of the participation of a particular atom to the vibrational mode. The magnitude of the displacement is represented by a sphere whose radius is proportional to the displacement (and are circles in a two dimensional plot). This type of plot for the 2 THz mode clearly shows that it is fully delocalized. All atoms within the molecule are displaced during the vibration.

These heat maps nicely illustrate which atoms contribute most to the resonance. A more quantitative approach is to decompose the mode into an intramolecular contribution, and an intermolecular one, which is further broken down into translational and rotational/librational components [19].

The results for the two strongest modes in L-carnosine, are plotted in Fig. 6. It is quite surprising that these low frequency modes have an intramolecular contribution of 50% to 60% because one would expect that the molecule is fairly rigid, but this behavior is actually fairly common. It is also seen that intermolecular contributions from translations and rotations/librations are fairly similar. These results illustrate the importance of utilizing periodic boundary conditions as only these will allow intermolecular movements in addition to intramolecular ones.

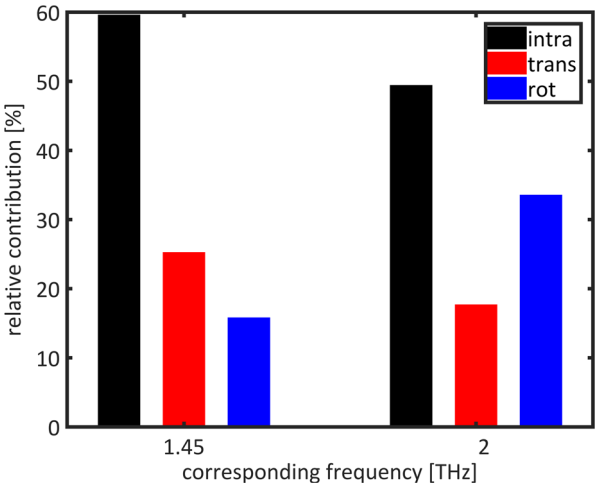

Fig. 6 Using Euler projection the relative contribution from inter molecular movements (translation and rotation) is separated from intra molecular movement. The contribution is roughly split 50/50, showcasing that periodic boundaries are of crucial important as gas phase would only cover the intra molecular contribution

6 Conclusion

We have presented THz spectra of the dipeptide L-carnosine at three different temperatures ranging from 300 to 65 K. We detected clear absorption resonances at 1.48 THz, 1.93 THz, and 2.27 THz which allow an unambiguous identification of the material. Additionally, we performed DFT calculations of the crystal. The calculated structure was in excellent agreement with experimental PXRD data. The calculated THz spectrum accurately reproduced the experimentally observed one. The results presented here demonstrate that DFT methods developed for crystals of monomeric amino acids can also be applied to larger dipeptide crystals.

Acknowledgments We thank Brandon Q. Mercado for measuring the powder XRD spectra, and Batop GmbH for providing the photoconductive antennas at a discount. JN also thanks Nikhil S. Malvankar for financial support.

Funding Information This study is financially supported by the National Science Foundation under grant no. NSF CHE—CSDMA 1465085.

Compliance with Ethical Standards

Conflict of Interest The authors declare that they have no conflict of interest.

References

1. E.C.B. Smith, The buffering of muscle in rigor; protein, phosphate and carnosine, J. Physiol. **92**(3), 336 (2019). https://doi.org/10.1113/jphysiol.1938.sp003605.
2. W. Derave, M.S. Özdemir, R.C. Harris, A. Pottier, H. Reyngoudt, K. Koppo, J.A. Wise, E. Achten, b-alanine supplementation augments muscle carnosine content and attenuates fatigue during repeated isokinetic contraction bouts in trained sprinters, J. Appl. Physiol. **103**(5), 1736 (2019). 10.1152/japplphysiol.00397.2007.
3. A.R. Hipkiss, Glycation, ageing and carnosine: Are carnivorous diets beneficial?, Mech. Ageing Dev. **126**(10), 1034 (2005). http://www.sciencedirect.com/science/article/pii/S0047637405001193.
4. P.J. Quinn, A.A. Boldyrev, V.E. Formazuyk, Carnosine: Its properties, functions and potential therapeutic applications, Molecular Aspects of Medicine **13**(5), 379 (1992). http://www.sciencedirect.com/science/article/pii/009829979290006L.
5. W. Withayachumnankul, D. Abbott, Metamaterials in the terahertz regime, IEEE Photon. J. **1**(2), 99 (2009).
6. M.A. Hoeh, J. Neu, K. Schmitt, M. Rahm, Optical tuning of ultra-thin, silicon-based flexible metamaterial membranes in the terahertz regime, Opt. Mater. Express **5**(2), 408 (2015). http://www.osapublishing.org/ome/abstract.cfm?URI=ome-5-2-408.
7. G. Acuna, S.F. Heucke, F. Kuchler, H.T. Chen, A.J. Taylor, R. Kersting, Surface plasmons in terahertz metamaterials, Opt. Express **16**, 23 (2008).
8. J. Neu, D.J. Aschaffenburg, M.R.C. Williams, C.A. Schmuttenmaer, Optimization of terahertz metamaterials for near-field sensing of chiral substances, IEEE Trans. THz Sci. Technol. **7**(6), 755 (2017). https://doi.org/10.1109/TTHZ.2017.2746259.
9. J. Neu, R. Beigang, M. Rahm, Metamaterial-based gradient index beam steerers for terahertz radiation, Appl. Phys. Lett. **103**(4), 041109 (2013). https://doi.org/10.1063/1.4816345.
10. H.T. Chen, W.J. Padilla, J.M.O. Zide, A.C. Gossard, A.J. Taylor, R.D. Averitt, Active terahertz metamaterial devices, Nature **444**(7119), 597 (2006). https://doi.org/10.1038/nature05343.

11. J. Neu, B. Krolla, O. Paul, B. Reinhard, R. Beigang, M. Rahm, Metamaterial-based gradient index lens with strong focusing in the THz frequency range, Opt. Express **18**(26), 27748 (2010). https://doi.org/10.1364/OE.18.027748. http://www.opticsexpress.org/abstract.cfm?URI=oe-18-26-27748.
12. M. Lu, J. Shen, N. Li, Y. Zhang, C. Zhang, L. Liang, X. Xu, Detection and identification of illicit drugs using terahertz imaging, J. Appl. Phys. **100**(10), 103104 (2006). https://doi.org/10.1063/1.2388041.
13. A.G. Davies, A.D. Burnett, W. Fan, E.H. Linfield, J.E. Cunningham, Terahertz spectroscopy of explosives and drugs, Mater. Today **11**(3), 18 (2008). https://doi.org/10.1016/S1369-7021(08)70016-6. http://www.sciencedirect.com/science/article/pii/S1369702108700166.
14. C. Zhang, K. Mu, X. Jiang, Y. Jiao, L. Zhang, Q. Zhou, Y. Zhang, J. Shen, G. Zhao, X.C. Zhang, in: *Proc. of SPIE*, vol. 6840 (2007), vol. 6840, p. 68400S.
15. H. Hoshina, Y. Sasaki, A. Hayashi, C. Otani, K. Kawase, Noninvasive Mail Inspection System with Terahertz Radiation, Appl. Spectrosc. **63**(1), 81 (2009). http://as.osa.org/abstract.cfm?URI=as-63-1-81.
16. T.M. Korter, R. Balu, M.B. Campbell, M.C. Beard, S.K. Gregurick, E.J. Heilweil, Terahertz spectroscopy of solid serine and cysteine, Chem. Phys. Lett. **418**(1), 65 (2006). http://www.sciencedirect.com/science/article/pii/S0009261405015988.
17. D.V. Nickel, M.T. Ruggiero, T.M. Korter, D.M. Mittleman, Terahertz disorder-localized rotational modes and lattice vibrational modes in the orientationally-disordered and ordered phases of camphor, Phys. Chem. Chem. Phys. **17**(10), 6734 (2015). https://doi.org/10.1039/C4CP04947K.
18. M.T. Ruggiero, J. Axel Zeitler, T.M. Korter, Concomitant polymorphism and the martensitic-like transformation of an organic crystal, Phys. Chem. Chem. Phys. **19**, 28502 (2017). https://doi.org/10.1039/C7CP04666A.
19. M.R.C. Williams, A.B. True, A.F. Izmaylov, T.A. French, K. Schroeck, C.A. Schmuttenmaer, Terahertz spectroscopy of enantiopure and racemic polycrystalline valine, Phys. Chem. Chem. Phys. **13**(24), 11719 (2011). https://doi.org/10.1039/C1CP20594C.
20. M. Walther, B.M. Fischer, P. Uhd Jepsen, Noncovalent intermolecular forces in polycrystalline and amorphous saccharides in the far infrared, Chemical Physics **288**(2), 261 (2003). http://www.sciencedirect.com/science/article/pii/S0301010403000314.
21. C.J. Strachan, P.F. Taday, D.A. Newnham, K.C. Gordon, J. Zeitler, M. Pepper, T. Rades, Using terahertz pulsed spectroscopy to quantify pharmaceutical polymorphism and crystallinity, Journal of Pharmaceutical Sciences **94**(4), 837 (2005). https://doi.org/10.1002/jps.20281. http://www.sciencedirect.com/science/article/pii/S0022354916317440.
22. M. Kawase, T. Saito, M. Ogawa, Uejima, Y. Hatsuda, S. Kawanishi, Y. Hirotani, M. Myotoku, K. Ikeda, H. Konishi, I.G.A. Ikumi, J. Yamakawa, S. Nishizawa, K. Yamamoto, T.A.N.I. Masahiko, Application of terahertz absorption spectroscopy to evaluation of aging variation of medicine:, Anal. Sci. **27**(2), 209 (2011).
23. J. Neu, C.T. Nemes, K.P. Regan, M.R.C. Williams, C.A. Schmuttenmaer, Exploring the solid state phase transition in dl-norvaline with terahertz spectroscopy, Phys. Chem. Chem. Phys. **20**, 276 (2018). https://doi.org/10.1039/C7CP05479C.
24. J. Neu, H. Nikonow, C.A. Schmuttenmaer, Terahertz spectroscopy and density functional theory calculations of dl-norleucine and dl-methionine, J. Phys. Chem. A (2018). https://doi.org/10.1021/acs.jpca.8b04978.
25. J. Neu, E.A. Stone, J.A. Spies, G. Storch, A.S. Hatano, B.Q. Mercado, S.J. Miller, C.A. Schmuttenmaer, Terahertz spectroscopy of tetrameric peptides, J. Phys. Chem. Lett. **10**(10), 2624 (2019). https://doi.org/10.1021/acs.jpclett.9b01091.
26. M.T. Ruggiero, W. Zhang, A.D. Bond, D.M. Mittleman, J.A. Zeitler, Uncovering the connection between low-frequency dynamics and phase transformation phenomena in molecular solids, Phys. Rev. Lett. **120**(19), 196002 (2018). https://doi.org/10.1103/PhysRevLett.120.196002.
27. T. Ruggiero Michael, S. Juraj, O. Roberto, Z.J. Axel, M. Korter Timothy, Measuring the elasticity of poly-l-proline helices with terahertz spectroscopy, Angew. Chem. Int. Ed. **55**(24), 6877 (2016). https://doi.org/10.1002/anie.201602268.
28. M.D. King, W.D. Buchanan, T.M. Korter, Understanding the terahertz spectra of crystalline pharmaceuticals: Terahertz spectroscopy and solid-state density functional theory study of (s)-(+)-ibuprofen and (rs)-ibuprofen, J. Pharm. Sci. **100**(3), 1116 (2011). https://doi.org/10.1002/jps.22339.
29. E.M. Witko, T.M. Korter, Investigation of the low-frequency vibrations of crystalline tartaric acid using terahertz spectroscopy and solid-state density functional theory, J. Phys. Chem. A **115**(35), 10052 (2011). https://doi.org/10.1021/jp204854e.

30. D.G. Allis, D.A. Prokhorova, T.M. Korter, Solid-state modeling of the terahertz spectrum of the high explosive hmx, J. Phys. Chem. A **110**(5), 1951 (2006). https://doi.org/10.1021/jp0554285.
31. M.R.C. Williams, D.J. Aschaffenburg, B.K. Ofori-Okai, C.A. Schmuttenmaer, Intermolecular Vibrations in Hydrophobic Amino Acid Crystals: Experiments and Calculations, J. Phys. Chem. B **117**(36), 10444 (2013).
32. A.B. True, K. Schroeck, T.A. French, C.A. Schmuttenmaer, Terahertz spectroscopy of histidine enantiomers and polymorphs, J. Infrared, Millimeter, Terahertz Waves **32**(5), 691 (2011). https://doi.org/10.1007/s10762-010-9645-9.
33. N.Y. Tan, M.T. Ruggiero, C. Orellana-Tavra, T. Tian, A.D. Bond, T.M. Korter, D. Fairen-Jimenez, J. Axel Zeitler, Investigation of the terahertz vibrational modes of zif-8 and zif-90 with terahertz time-domain spectroscopy, Chem. Commun. **51**, 16037 (2015). https://doi.org/10.1039/C5CC06455D.
34. J. Neu, C.A. Schmuttenmaer, Tutorial: An introduction to terahertz time domain spectroscopy (thz-tds), J. Appl. Phys. **124**(22), 231101 (2018). https://aip.scitation.org/doi/full/10.1063/1.5047659.
35. V.A. Markel, Introduction to the maxwell garnett approximation: tutorial, J. Opt. Soc. Am. A **33**(7), 1244 (2016). http://josaa.osa.org/abstract.cfm?URI=josaa-33-7-1244.
36. D.A.G. Bruggeman, Berechnung verschiedener physikalischer konstanten von heterogenen substanzen. i. dielektrizitätskonstanten und leitfähigkeiten der mischkörper aus isotropen substanzen, Ann. Phys. **416**(7), 636 (1935). https://doi.org/10.1002/andp.19354160705.
37. H. Itoh, T. Yamane, T. Ashida, M. Kakudo, Carnosine (β-alanyl-L-histidine), Acta Crystallographica Section B **33**(9), 2959 (1977). https://doi.org/10.1107/S0567740877009972.
38. J.F. Federici, B. Schulkin, F. Huang, D. Gary, R. Barat, F. Oliveira, D. Zimdars, Thz imaging and sensing for security applications-explosives, weapons and drugs, Semicond. Sci. Technol. **20**(7), S266 (2005). http://stacks.iop.org/0268-1242/20/i=7/a=018.
39. M.D. King, W.D. Buchanan, T.M. Korter, Identification and quantification of polymorphism in the pharmaceutical compound diclofenac acid by terahertz spectroscopy and solid-state density functional theory, Anal. Chem. **83**(10), 3786 (2011). https://doi.org/10.1021/ac2001934.
40. A.J. Zeitler, T.F. Philip, A. Newnham David, M. Pepper, G.C. Keith, T. Rades, Terahertz pulsed spectroscopy and imaging in the pharmaceutical setting - a review, J. Pharm. Pharmacol. **59**(2), 209 (2007). https://doi.org/10.1211/jpp.59.2.0008.
41. J.M. Soler, E. Artacho, J.D. Gale, A. García, J. Junquera, P. Ordejón, D. Sánchez-Portal, The siesta method for ab initio order- n materials simulation, J. Phys.: Condens. Matter **14**(11), 2745 (2002). http://stacks.iop.org/0953-8984/14/i=11/a=302.
42. K. Berland, P. Hyldgaard, Exchange functional that tests the robustness of the plasmon description of the van der waals density functional, Phys. Rev. B **89**(3), 035412 (2014). https://link.aps.org/doi/10.1103/PhysRevB.89.035412.
43. M. Dion, H. Rydberg, E. Schröder, D.C. Langreth, B.I. Lundqvist, Van der waals density functional for general geometries, Phys. Rev. Lett. **92**(24), 246401 (2004). http://link.aps.org/doi/10.1103/PhysRevLett.92.246401.
44. A.B. True, K. Schroeck, T.A. French, C.A. Schmuttenmaer, Terahertz spectroscopy of histidine enantiomers and polymorphs, J. Infrared, Millimeter, Terahertz Waves **32**(5), 691 (2011).
45. R.D. King-Smith, D. Vanderbilt, Theory of polarization of crystalline solids, Phys. Rev. B **47**(3), 1651 (1993). http://link.aps.org/doi/10.1103/PhysRevB.47.1651.
46. D. Fernández-Torre, R. Escribano, T. Archer, J.M. Pruneda, E. Artacho, First-principles infrared spectrum of nitric acid and nitric acid monohydrate crystals, J. Phys. Chem. A **108**(47), 10535 (2004). https://doi.org/10.1021/jp047249d.
47. P.M. Hakey, D.G. Allis, M.R. Hudson, W. Ouellette, T.M. Korter, Terahertz spectroscopic investigation of s-(+)- ketamine hydrochloride and vibrational assignment by density functional theory, J. Phys. Chem. A **114**(12), 4364 (2010). https://doi.org/10.1021/jp910861m.